Vortex Structure of a Synthetic Jet Issuing into a Turbulent Boundary Layer from a Finite-span Rectangular Orifice

Randy Belanger*, David W. Zingg†, and Philippe Lavoie‡
University of Toronto, Toronto, Ontario, M3H 5T6, Canada

The vortical structures formed during the expulsion stroke of synthetic jet actuation depend upon both the amplitude and the frequency of the actuation. Much work has been done to characterize jets ejected through circular orifices in crossflow, but less has been done for synthetic jets ejected through finite-span rectangular orifices. Implicit large-eddy simulation is used to elucidate the synthetic jet vortical structures issuing from a finite-span rectangular orifice into a turbulent boundary layer for a range of synthetic jet frequencies and blowing ratios. The evolution of the vortical structures near the jet orifice shows small horseshoe-shaped structures initially forming at the edges of the jet at moderate to high frequencies and low blowing ratios, similar to in quiescent conditions. These either coalesce to form a large horseshoe structure downstream, or partially break down to form a streamwise vortex pair at the edges of the orifice. At lower frequencies, the expulsion stroke is longer and the downstream vortex gets stretched downstream before forming a horsehoe-shaped vortical structure. At higher blowing ratios, the near field evolution is very similar to the ejection of the jet into quiescent flow; however, the presence of the crossflow prevents it from fully developing and stretches the vortical structures downstream, forming many different structures.

I. Nomenclature

AR	orifice aspect ratio
a	quiescent speed of sound
a_∞	freestream speed of sound
D	velocity gradient tensor
f	frequency
f_{sj}	computational frequency
h	smallest dimension of synthetic jet orifice
L	stroke length
l_x	streamwise length of computational domain
l_y	wall-normal length of computational domain
l_z	spanwise length of computational domain
M_∞	freestream Mach number
M_{jet}	jet Mach number
N_{tot}	total number of nodes
N_x	number of nodes in streamwise direction
N_y	number of nodes in wall-normal direction
N_z	number of nodes in spanwise direction
Q	second-invariant of velocity gradient tensor
Re_θ	momentum thickness Reynolds number
$\mathrm{Re}_{U_{\text{jet}}}$	jet Reynolds number
r	blowing ratio
S	strain-rate tensor
St	quiescent Strouhal number

*PhD Candidate, Institute for Aerospace Studies, randy.belanger@utoronto.ca.
†University of Toronto Distinguished Professor of Computational Aerodynamics and Sustainable Aviation, Institute for Aerospace Studies, dwz@utias.utoronto.ca, AIAA Associate Fellow.
‡Professor, Institute for Aerospace Studies, lavoie@utias.utoronto.ca, AIAA Associate Fellow.

St_∞	crossflow Strouhal number
t	nondimenstional time
U	mean streamwise velocity
U_∞	freestream velocity
U_{jet}	averaged jet expulsion velocity
U_{peak}	peak jet expulsion velocity
u_τ	friction velocity
u'_{rms}	rms fluctuating streamwise velocity
$\tilde{u}_{\mathrm{jet}}$	phase-averaged jet velocity
V_{peak}	maximum wall-normal jet velocity boundary condition
v	wall-normal velocity
v_{peak}	wall-normal jet velocity boundary condition
w	spanwise dimension of the synthetic jet orifice
x	streamwise coordinate
y	wall-normal coordinate
z	spanwise coordinate
x^*	shifted streamwise coordinate
z^*	shifted spanwise coordinate
Δt	nondimensional time step
Δx^+	streamwise spacing in inner units
Δy^+	wall-normal spacing in inner units
Δz^+	spanwise spacing in inner units
δ	boundary-layer thickness
δ_0	boundary-layer thickness at midpoint of computational domain
ϕ	phase
ν	kinematic viscosity
Ω	vorticity tensor

II. Introduction

For certain applications of engineering interest, where the use of synthetic jets in a crossflow can be employed, it is preferred to match the size of the jet orifice to the length scales of certain structures in the flow without having a large orifice cross-sectional area. One particular example is friction drag reduction, where it may be beneficial to have an orifice size that matches either large spanwise or streamwise scales in a turbulent boundary layer. A synthetic jet actuator with a finite-span rectangular orifice is well suited for such applications.

The frequency and amplitude of a synthetic jet issuing into a crossflow can be represented by a non-dimensional Strouhal number St_∞, blowing ratio r, and, by combining them, a nondimensional stroke length L/h:

$$\mathrm{St}_\infty = \frac{fh}{U_\infty}, \quad r = \frac{U_{\mathrm{jet}}}{U_\infty}, \quad \frac{L}{h} = \frac{r}{\mathrm{St}_\infty}. \tag{1}$$

Here f is the frequency of actuation, h is the smallest dimension of the jet orifice, U_∞ is the free-stream velocity, and U_{jet} is the expulsion jet velocity averaged over the entire jet cycle:

$$U_{\mathrm{jet}} = \frac{1}{2\pi}\int_0^\pi \tilde{u}_{\mathrm{jet}}(\phi)\mathrm{d}\phi = \frac{U_{\mathrm{peak}}}{\pi}, \tag{2}$$

where $\tilde{u}_{\mathrm{jet}}(\phi)$ is the phase-averaged jet velocity, ϕ is the phase, U_{peak} is the peak jet velocity, and the second equality holds only for a sinusoidal jet velocity. We can also define a jet Reynolds number using the jet velocity defined above and the width of the orifice:

$$\mathrm{Re}_{U_{\mathrm{jet}}} = \frac{U_{\mathrm{jet}}h}{\nu}, \tag{3}$$

where ν is the kinematic viscosity.

Much work has been done in the past to characterize the vortical structure emitted by jets in a crossflow. These include steady jets (jets with long-duration blowing), pulsed jets (jets with short-duration blowing), and synthetic jets

(jets with periodic blowing and suction). Steady jets in crossflow have been studied extensively; Fric & Roshko [1] provide a comprehensive model for their vortex structure when formed through a circular orifice in a laminar crossflow. The model consists of a counter-rotating vortex pair in the far-field, jet shear-layer vortices forming on the inclined portion of the jet in the near-field, a horseshoe-shaped vortex wrapping around the upstream side of the orifice, and vertical vortices formed in the wake of the jet which are attached to the wall and the underside of the counter-rotating vortex pair. For pulsed jets, Sau & Mahesh [2] constructed a parameter map detailing the vortical structures of synthetic jets emitted through a circular orifice in a laminar crossflow. At low blowing ratio, the vortical structure involves a shedding of hairpin vortices. At higher blowing ratio, the vortical structure either forms a tilted, isolated vortex ring; or a tilted vortex ring with a trailing column of fluid. The vortex ring is inclined in the streamwise direction for the former and declined for the latter.

The structure of synthetic jets in the near-field without a crossflow can be described as a train of vortex rings. As the jet propagates further away from the orifice, though, the structure can take different forms depending on the frequency and amplitude of the actuation, as is shown by Cater and Soria [3] for a circular orifice. At a low enough frequency, the vortex rings that are emitted by successive cycles remain separated, and a train of vortex rings prevails further away from the orifice. At higher frequencies, successive vortex rings merge and form a laminar, transitional, or turbulent jet depending on the Reynolds number of the jet. Additionally, in the near-field, over one synthetic jet cycle, there exists either an isolated vortex ring or a vortex ring with a trailing column of fluid. The trailing column of fluid forms when the vortex ring has reached a maximum circulation. This appears to happen at an L/h of around 4 for circular pulsed and synthetic jets, where secondary vortical structures are formed in the trailing jet column at higher stroke lengths [4, 5]. Sau & Mahesh [2] showed that this 'formation number' changes with the blowing ratio when using a circular pulsed jet in crossflow. At low blowing ratios, the formation number is smaller than is seen in quiescent conditions, but as the blowing ratio is increased, the formation number approaches the quiescent formation number. Finally, in order for a vortex ring formed during the expulsion half of the cycle to survive the subsequent suction, it must travel far enough away from the orifice during the expulsion stroke. This is known as the formation criterion and has also been shown to depend on the stroke length [6]. For synthetic jets formed through circular orifices, this criterion is approximately $L/d > 0.5$, where d is the diameter of the orifice. For two-dimensional jets, this criterion increases to roughly $L/h > 3$. The criterion for finite-span rectangular orifices likely lies somewhere between the two and depends on the orifice aspect ratio.

In a laminar crossflow, and for a circular orifice, Jabbal & Zhong [7] constructed a parameter map for the different vortical structures that are formed with a synthetic jet actuator. At low stroke length and blowing ratio, the synthetic jet consists of a single hairpin vortex, whereas at increasing stroke length and blowing ratio, the structure is that of a stretched vortex ring, and then a tilted and distorted vortex ring. However, notable areas of the parameter map remain unexplored, in particular small stroke lengths at high blowing ratio and large stroke lengths with low blowing ratio.

No comprehensive study has been conducted to elucidate the vortical structure of synthetic jets issued through rectangular orifices having a finite-span in a laminar crossflow, let alone in a turbulent crossflow, under a wide range of actuation conditions. Van Buren et al. [8] studied the structure of synthetic jets emitted through a finite-span rectangular orifice using particle image velocimetry in a laminar boundary layer. Their results showed that the dominant vortical structure formed is a pair of quasi-steady streamwise vortices for all cases that they tested. However, Van Buren et al. focused on a narrow set of parameters, leaving much of the parameter space unexplored. Sahni et al. [9] also studied synthetic jets issued from a finite-span orifice (with aspect ratio 21.33) in laminar crossflow on a NACA 4421 airfoil. They tested blowing ratios ranging from 0.2–1.2 (with a focus on 0.4 and 1.2) and at a single frequency having $\mathrm{St}_\infty = 0.1875$. While they did not look at the complete vortical structure, and concentrated on a fairly small streamwise domain close to the orifice, they did provide information on the spanwise vorticity and cross-stream velocity field. They show that at $r = 0.4$ the initial upstream spanwise vortex is killed by the mean shear and that the remaining spanwise vorticity from the downstream vortex roller remains close to the wall with successive cycles causing a wave-like undulation in the boundary layer vorticity. At higher r, however, they show that the upstream roller survives the mean shear, rotates over the downstream roller from the same cycle, and its upwash causes lift-up of the vortex from the previous cycle further downstream. Furthermore, at $r = 0.4$, their results show that additional streamwise vorticity arises downstream of the orifice at the edges of the jet, aside from the initial streamwise vortex formed during the expulsion stroke. They conjecture that this is due to secondary vortex structures, such as those seen in the experiments of Amitay & Cannelle [10] and Van Buren et al. [11]. These secondary structures are seen as regions of counter-rotating vorticity closer to the centerline of the main vortex ring in planes along the long-axis of the jet. Furthermore, both Amitay & Cannelle and Van Buren et al. found that the number of these secondary structures increases with the aspect ratio. One possible explanation is that spanwise waviness in the main vortex ring induces secondary rib-like structures,

Table 1 Details of the computational mesh.

	l_x	l_y	l_z	N_x	N_y	N_z	N_{tot}	Δx^+	Δy^+_{min}	Δy^+_{max}	Δz^+
	$20\delta_0$	$4\delta_0$	$3\delta_0$	545	161	289	$25.4{\times}10^6$	28	0.44	47	8.0
slot	$0.023\delta_0$	$0.075\delta_0$	$0.3\delta_0$	13	65	33	$2.78{\times}10^4$	1.5	0.44	1.5	7.0

similar to those seen by Smith & Glezer [12] for a synthetic jet issuing through a large aspect ratio orifice, due to an instability related to the aspect ratio of the orifice.

The goal of this study is to understand the vortical structures produced by a synthetic jet actuator having a rectangular orifice as a function of the actuation parameters in order to aid future flow control studies. Of particular interest is the potential to tailor the structures produced by the synthetic jet actuator to the application. In what follows we study the effect of the actuation frequency and amplitude on the emitted vortical structures from a finite-span rectangular orifice into a turbulent boundary layer using large eddy simulation.

The flow structures introduced into the boundary layer by the synthetic jet actuator are visualized using positive isocontours of Q, which is the second invariant of the velocity gradient tensor:

$$Q = \frac{1}{2}\left(||\Omega||^2 - ||S||^2\right), \tag{4}$$

where Ω and S are the vorticity and strain-rate tensor, respectively, and $||\cdot||$ denotes a 2-norm. These are also, respectively, the antisymmetic and symmetric parts of the velocity gradient tensor, D_{ij}, such that:

$$D_{ij} = \frac{\partial u_i}{\partial x_j} = \Omega + S. \tag{5}$$

Values of positive Q thus represent locations where vortical motions are dominant. In the figures to follow, Q is nondimensionalized with the reference velocity and length scales of the simulations.

III. Computational Setup

Simulations of the turbulent boundary layer and synthetic jet were performed using implicit large-eddy simulation (ILES) with the compressible finite-difference flow solver DIABLO. For details on the flow solver see Refs.[13, 14], and for details on the implementation of ILES in the flow solver see Ref.[15]. This solver utilizes a parallel Newton-Krylov-Schur solution algorithm on a multiblock mesh. Globally 4th-order summation-by-parts operators are used to discretize the grid with simultaneous approximation terms to weakly enforce boundary and interface conditions. In addition, numerical dissipation is added to stabilize the solution by dissipating under-resolved high-frequency modes. A 2nd-order explicit-first-stage singly-diagonally-implicit Runge-Kutta method is used to march forward in time. The reference length scale is δ_0, the boundary-layer thickness at the streamwise-midpoint of the computational domain, and the reference velocity scale is the freestream speed of sound a_∞. All simulations were conducted with the turbulent boundary layer crossflow having a freestream Mach number of $\mathrm{M}_\infty = 0.2$, with a momentum thickness Reynolds number of $\mathrm{Re}_\theta = 2520$ ($\mathrm{Re}_\tau = 770$).

A rectilinear grid was used with nominally uniform spacing in the streamwise and spanwise directions, and hyperbolic tangent spacing in the wall-normal direction. The dimensions, number of nodes, and spacing in each of the coordinate directions are described in Table 1. For parallelization the grid is split into blocks containing nominally 33^3 nodes each, which are assigned to a separate processor. One additional block is used for the synthetic jet slot as described below. Thus, there are a total of 766 blocks. The block structure of the grid is shown in Fig. 1a.

In the streamwise direction, we use the rescale/recycle procedure of Lund et al. [16] to generate turbulence at the inflow boundary; a recycle plane at $x = 7.5\delta_0$ is used to rescale turbulence statistics and recycle them back to the inflow boundary. At outflow we use a convective boundary condition, where the convection velocity is calculated at $x = 17.5\delta_0$. At the bottom of the domain ($y = 0$), we use an adiabatic no-slip boundary condition to simulate a flat plate, while at the top of the domain the solution is extrapolated from the solution in the interior of the domain. Finally, the spanwise planes are periodic.

For controlled turbulent boundary-layer simulations, the synthetic jet actuator is modelled as a slot extruded below the wall at the streamwise and spanwise midpoint of the computational domain, as shown in Fig. 1b. The grid is also

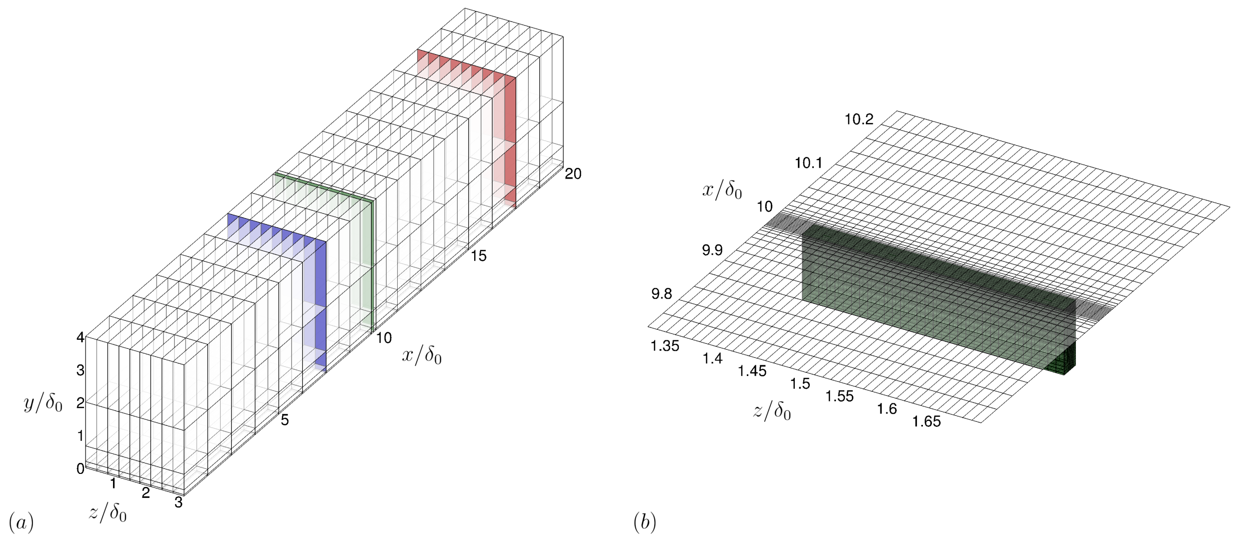

Fig. 1 (a) Block structure of the computational domain, with the recycle plane (blue), reference plane for convective outflow (red), and streamwise location of the synthetic jet slot (green). Each block includes 33 nodes in each dimension except for the block containing the synthetic jet slot, which is described in Table 1. (b) The computational mesh for the synthetic jet slot, indicated in green, and surface plane ($y/\delta_0 = 0$) in the vicinity of the slot.

refined in the streamwise and spanwise directions in the vicinity of the jet slot to provide finer grid spacing in the slot. The rectangular orifice is spanwise oriented, measuring $0.3\delta_0$ in z with an aspect ratio of 13. At the base of the slot is a wall-normal velocity boundary condition with a trapezoidal shape in both the x and z directions, where the peak jet velocity exists over 90% of the slot and tapers linearly to zero at the edges in the x direction. In the larger z direction, the tapered region is kept the same size as the x direction. Previous simulations by Raju et al. [17] have shown that modelling the jet as a slot with a velocity boundary condition represents a synthetic jet with sufficient accuracy, while reducing the numerical cost of simulating the entire actuator. The peak wall-normal velocity at the base of the slot is oscillated sinusoidally as:

$$v_{\text{peak}}(t) = V_{\text{peak}} \sin(f_{\text{sj}} t) \tag{6}$$

where $f_{\text{sj}} = 2\pi \text{St}_\infty \text{M}_\infty$ is the synthetic jet frequency, t is the nondimensional time, and $V_{\text{peak}} = \pi r \text{M}_\infty$ is the maximum peak wall-normal velocity.

The time step is adjusted for each case such that the solution is computed at 100 points per cycle of the synthetic jet. The full solution was saved at every 10th time step with phase-averages computed as 10 separate ensemble averages over these 10 points in the cycles.

For quiescent jet simulations, the grid is scaled on the width of the synthetic jet actuator orifice, and the velocity is scaled using the speed of sound a. A jet Mach number, defined as $M_{\text{jet}} = U_{\text{jet}}/a$, is set at a value of 0.1 and is used to set the Reynolds number and frequency of actuation. The domain for these simulations is $50h$ in each of the three dimensions and the nominal grid spacing matches a similar region in the crossflow simulations.

IV. Results

A. Baseline Turbulent Boundary Layer

The simulations of the turbulent boundary layer under synthetic jet actuation were warm-started from a simulation of a baseline turbulent boundary layer flow on a similar grid with the same numerical dissipation coefficients, but without the synthetic jet slot. This simulation was run for about $2000\delta/a_\infty$ time units in order to remove transients associated with the turbulence generation procedure and reach an adequately converged turbulent boundary-layer flow. Furthermore, the time step was slowly ramped up to $\Delta t = 1.0\delta/a_\infty$ at $t = 1000\delta/a_\infty$ in order to remove these transients quickly. The time step was subsequently reduced to minimize error in the solution. The mean and fluctuating streamwise

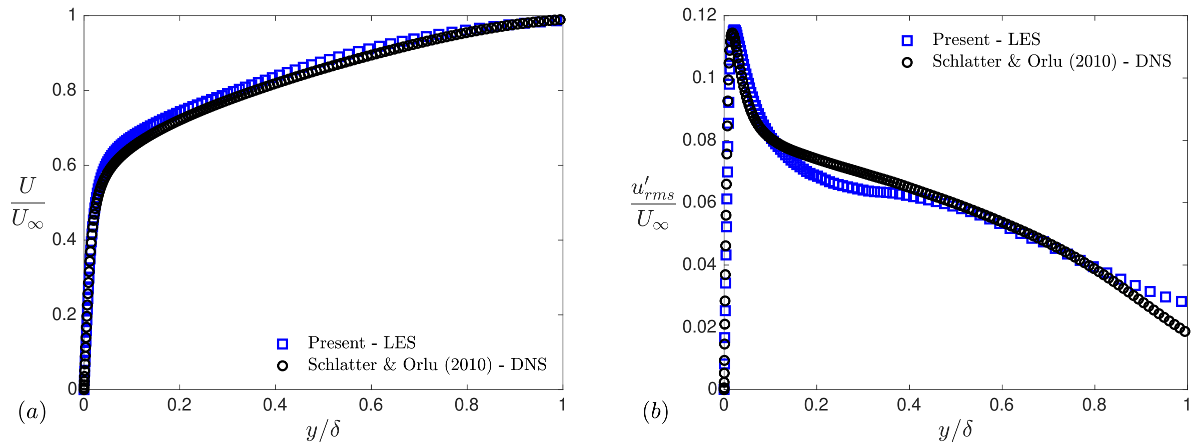

Fig. 2 Boundary layer profile of (a) streamwise mean velocity, and (b) streamwise rms velocity fluctuations on a linear scale. DNS data, taken from Schlatter & Örlu [18], are plotted for comparison.

velocity profiles of the baseline flow are shown in Fig. 2 in outer units on a linear scale. These boundary layer profiles are at $x/\delta_0 = 10$: the location of the synthetic jet slot in the controlled simulations. The mean and fluctuating streamwise velocity profiles of the direct numerical simulation (DNS) of Schlatter & Örlu ($\mathrm{Re}_\theta = 2540$) [18] are also included in Fig. 2 for comparison. The near-wall region of our ILES matches closely with the DNS for both the mean and fluctuating u. Only in the log-region of the fluctuating velocity profile is there a small departure from the DNS, where we slightly underpredict the strength of the fluctuations. There is also excess turbulence at the top of the boundary layer and freestream compared to DNS. As the mean flow is believed to be the main driver of the vortical structures in crossflow, we have confidence that the propagation of the structures in turbulent crossflow will be accurate based on our agreement with DNS.

The Reynolds number of many engineering applications of interest is typically much higher than is possible for direct numerical simulation, and even large eddy simulation. The choice of grid and Reynolds number was based on a tradeoff between higher Reynolds number and the computational cost associated with simulating a turbulent boundary layer at such a Reynolds number for a large number of cases, while maintaining a reasonable degree of accuracy. It has been shown that the trajectory of a streamwise-aligned jet is only weakly impacted by the Reynolds number [19]. A spanwise-aligned jet, showing a larger cross-section to the oncoming flow than a streamwise-aligned jet, does not penetrate as far into the boundary layer and is thus more susceptible to changes in the boundary-layer Reynolds number [20]. Nevertheless, we anticipate that the effect of the Reynolds number will be secondary to the effect of the actuation parameters, r and St_∞, on the flow structures.

B. Jet Flow

The variation of the phase-averaged wall-normal jet velocity with phase is shown in Fig. 3a. This is extracted at the orifice exit (i.e., $y = 0$), and at the centre of the slot in the streamwise and spanwise dimensions for a case with $r = 0.3$ and $\mathrm{St}_\infty = 0.1$. This is chosen rather than a spatially-averaged velocity over the slot because the jet velocity varies throughout the slot, as can be seen in Fig. 3b. The red dashed line in Fig. 3a indicates the sinusoidal input waveform introduced at the base of the synthetic jet slot, as in Eq. (6). Additionally, the point corresponding to $\phi = 0°$ is repeated at $\phi = 360°$. There does not appear to be much difference between the input waveform and what is detected at the centerline of the orifice exit. The only apparent difference is a slight phase-shift due to the length of the slot. This phase-shift is more prominent during the suction half of the cycle. Since we have only phase-averaged for 10 phases in the cycle, we only have 10 jet velocity data points. Thus, it is possible that there is more difference with the input signal, such as a smaller vortex formation peak before the expulsion peak [12], that is not being captured.

The phase-averaged output of the jet for the same case as Fig. 3a at the orifice exit in crossflow is shown in Fig. 3b along both the streamwise and spanwise directions. This is shown for the first measured phase after maximum expulsion ($\phi = 104°$) because this is the phase closest to maximum expulsion, as seen in Fig. 3a. We have introduced shifted coordinates in Fig. 3b so that the centre of the slot orifice is located at the origin of this coordinate system. There is

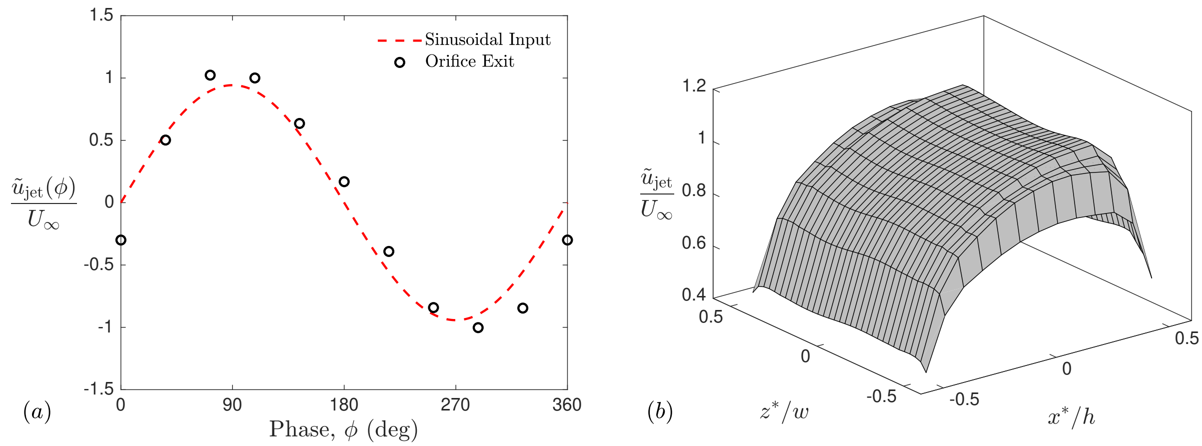

Fig. 3 Variation of (a) phase-averaged wall-normal velocity at the jet orifice centerline with phase, and (b) phase-averaged wall-normal velocity with both scaled streamwise and spanwise length at peak blowing ($\phi = 104°$). These are both extracted during crossflow at the orifice exit ($y = 0$) for a case with $r = 0.3$ and $\mathrm{St}_\infty = 0.1$.

variation in both the streamwise and spanwise directions. The crossflow causes the distribution of the jet velocity at the orifice to weaken upstream and strengthen downstream. This has been seen previously in the DNS of Ravi et al. [21], where they show that the magnitude of the skew may also be weakly related to the aspect ratio of the slot. This is also seen in the DNS of Sau & Mahesh [2], where they show that the skew depends on the blowing ratio of a pulsed jet. There are also additional peaks in the jet velocity at the edges of the slot in the spanwise direction, which are due to the presence of a rectangular vortex ring (which has its strongest uplift of fluid at the spanwise edges due to the confluence of spanwise and streamwise vorticity). The experimental results of Amitay & Cannelle [10] show a similar spanwise distribution of wall-normal velocity in the absence of crossflow, which they show depends on the jet velocity (or stroke length) for a fixed frequency and aspect ratio; on the aspect ratio of the jet, where they show the edge peaks are more prominent for smaller aspect ratios; and on the Reynolds number of the jet, with a higher Reynolds number giving a more rounded profile with less prominent peaks near the edges of the orifice.

These results show that the simulated synthetic jet flow at the orifice exit matches the sinusoidal input velocity that is input at the base of the slot, and that the velocity distribution matches, on a qualitative level, what has been seen in previous simulations and experiments. This adds confidence to the accuracy of the approach taken to simulating the synthetic jet flow.

C. Synthetic Jet Issuing into Quiescent Flow

Simulations were performed for a few cases with the synthetic jet issuing into a quiescent flow to understand the effect of grid density on the vortical structures that form at the orifice and propagate downstream. In particular, we were interested to see if, by increasing the number of nodes, there would be smaller-scale regular vortical structures formed that are not captured using a coarser mesh. The relevant nondimensional parameters for a synthetic jet in quiescent flow are the Strouhal number and the Reynolds number of the jet. As there is no crossflow, the Strouhal number is scaled based on the average jet velocity in Eq. (2), rather than U_∞: $\mathrm{St} = fh/U_{\rm jet}$. In Fig. 4 we show the vortical structures that emerge for two different forcing conditions (St, $\mathrm{Re}_{U_{\rm jet}}$): (0.19, 191) and (0.063, 574), and with a grid matching the grid in the vicinity of the jet slot in the crossflow simulation (nominal grid) and another with twice the number of nodes in each direction. The difference in St is due to an increase in $U_{\rm jet}$, and in crossflow this would result in the same St_∞, but with an r three times larger. The two $\mathrm{Re}_{U_{\rm jet}}$ are chosen to match the smallest and largest r in the crossflow simulations, and the St is chosen to match $\mathrm{St}_\infty \approx 0.1$ in crossflow. While the finer grid more finely resolves the vortical structures for both cases in Fig. 4, there does not appear to be any additional regular vortical structures present. Reducing the isocontour value for Q, and thereby allowing weaker vortical structures, does not increase the number of regular vortices. However, this is not wholly unexpected. While secondary smaller-scale vortices have been seen in the work of Smith & Glezer [12] and Amitay & Cannelle [10], whereby smaller vortex 'ribs' wrap around the primary vortex ring, both of these studies involved the use of a much larger orifice aspect ratio ($AR = 150$ and

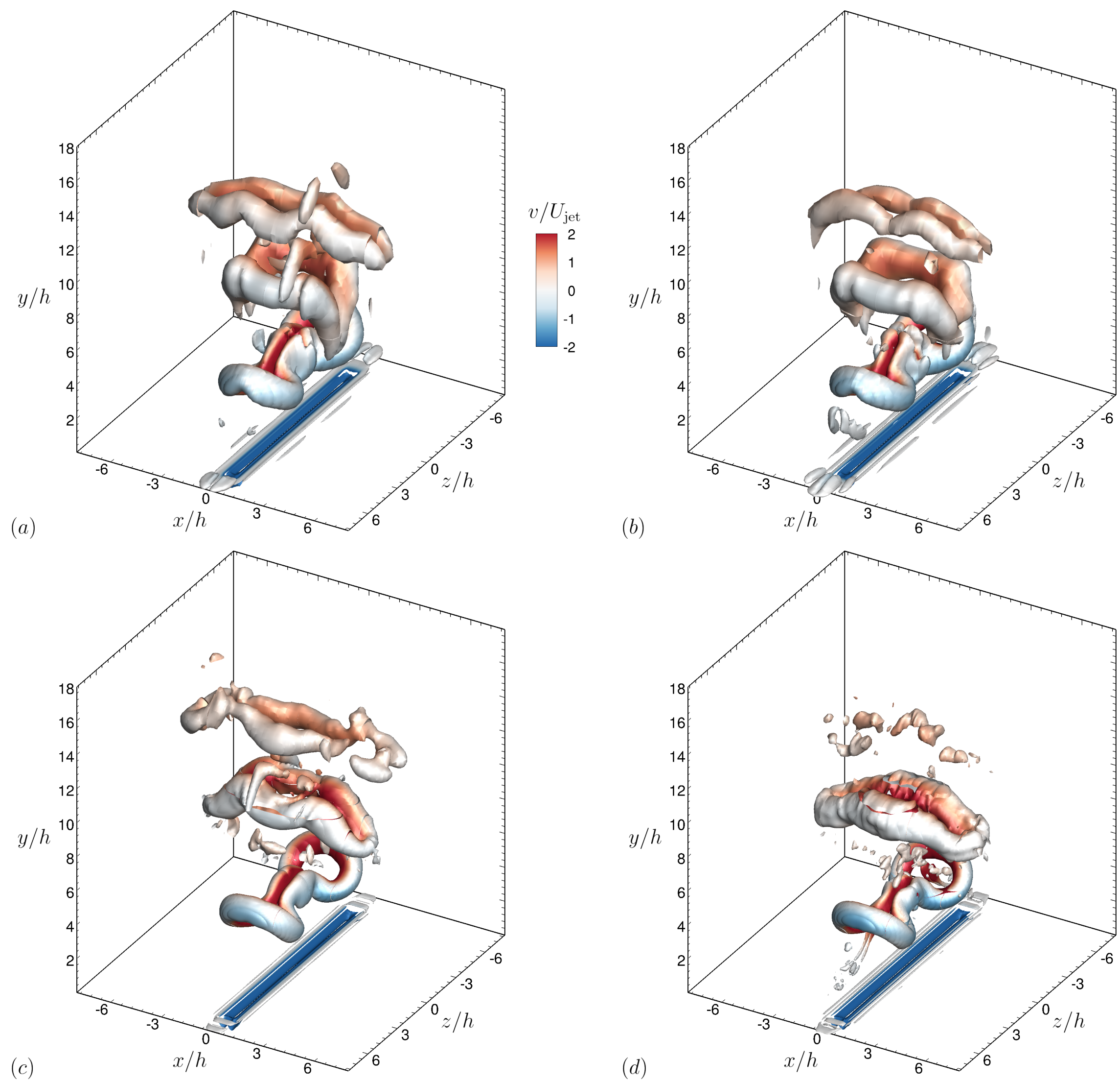

Fig. 4 Phase-averaged $Q = 0.001$ **isocontour at** $\phi = 324°$ **for the (a, c) nominal grid, and (b, d) fine grid for the (a, b)** St $= 0.19$, $\mathrm{Re}_{U_{\rm jet}} = 191$ **case and (c, d)** St $= 0.063$, $\mathrm{Re}_{U_{\rm jet}} = 574$ **case.**

AR = 50–100, respectively). Furthermore, Van Buren et al. [11] compared the effect of orifice aspect ratio on synthetic jets issuing into quiescent flow and found that additional vorticity appears inside the main vortex ring in a centerline plane along the long-axis of the orifice with AR = 18, but not for AR = 12 and AR = 6. Thus, we are confident that the nominal grid has a satisfactory resolution to adequately resolve the entire periodic vortical structure emitted by the actuator without missing smaller-scale secondary vortices.

There is additional information that we can extract from these simulations. For example, there is not much difference between the two cases with different St and $\mathrm{Re}_{U_{\rm jet}}$. For a constant viscosity, the difference between the two is a threefold increase in jet velocity, as stated above. This seems to indicate that the vortical structures are not particularly dependent on the jet velocity in quiescent flow. However, as we will show below, this is not the case when these same jets are put in a turbulent boundary layer crossflow due to the higher level of penetration with increased jet velocity, or blowing ratio. Furthermore, these simulations allow us to see how the vortex ring develops as it propagates downstream (along the jet axis), including its axis switching, as in Fig. 5. In Fig. 5a, initially a vortex ring is formed at all four edges of the orifice. The confluence of x and z vorticity at the short edges of the ring results in a stronger induced velocity, which tilts the vortex ring upwards compared to the center of the ring. As this ring propagates downstream, it shrinks along the long axis and grows along the short axis (Fig. 5(b-d)). Eventually these lifted up edges are pulled up near the jet centerline

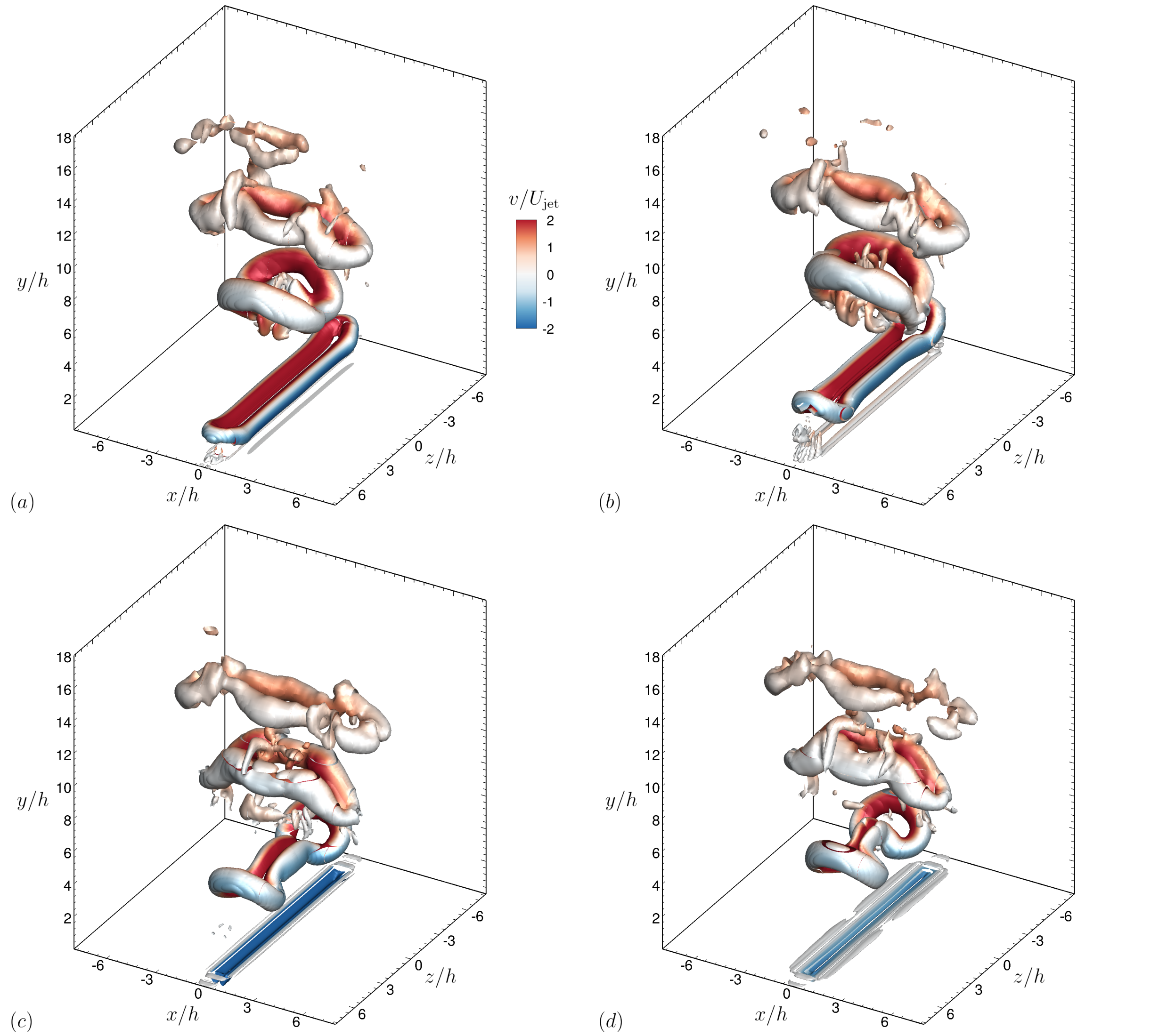

Fig. 5 Phase-averaged $Q = 0.001$ **isocontours for the** $\mathrm{St} = 0.19$**,** $\mathrm{Re}_{U_{\mathrm{jet}}} = 191$ **case at: (a)** $\phi = 108°$**, (b)** $\phi = 180°$**, (c)** $\phi = 288°$**, and (d)** $\phi = 360°$**.**

and form the central portion of a ring that is aligned along z rather than x (see the second vortex ring in Fig. 5(a-d)). The development, and axis switching, of the vortex ring seen here matches up very well with previous PIV experiments [11].

According to Chen et al. [22], for a synthetic jet with an orifice aspect ratio of 71, transition occurs around $\mathrm{Re}_{U_{\mathrm{jet}}} = 100$ for jets with a stroke length $L/h = 1/\mathrm{St} < 8$. At higher L/h, they show that the transition moves to increasingly lower $\mathrm{Re}_{U_{\mathrm{jet}}}$. Based on this, the Reynolds numbers chosen should roughly correspond to a transitional jet ($\mathrm{Re}_{U_{\mathrm{jet}}} = 191$) and a turbulent jet ($\mathrm{Re}_{U_{\mathrm{jet}}} = 574$). This is evidenced in Fig. 6, which shows instantaneous isocontours of Q after 50 cycles of synthetic jet actuation immediately preceding the end of the blowing cycle for the fine grid case. As can be seen, for the low $\mathrm{Re}_{U_{\mathrm{jet}}}$ case, there is only a moderate amount of turbulence that seems to develop further away from the orifice, while for the higher $\mathrm{Re}_{U_{\mathrm{jet}}}$ case there are a significant number of small-scale vortical structures corresponding to a turbulent jet.

D. Effect of Strouhal Number and Blowing Ratio on Vortex Structure in Crossflow

Simulations were conducted at three Strouhal numbers ($\mathrm{St}_\infty = \{0.01, 0.05, 0.1\}$) and three blowing ratios ($r = \{0.3, 0.6, 0.9\}$). These blowing ratios result in jet Reynolds numbers of $\mathrm{Re}_{U_{\mathrm{jet}}} = \{191, 382, 574\}$, which are transitional and

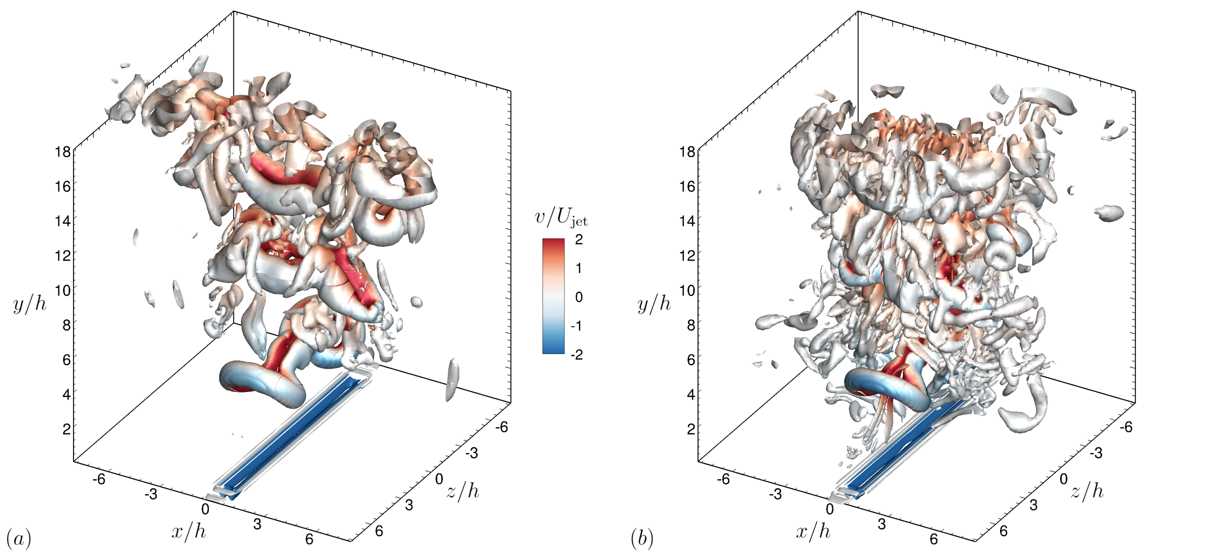

Fig. 6 Instantaneous phase-averaged $Q = 0.001$ **isocontour at** $\phi = 324°$ **after about 50 jet cycles for the (a)** St = 0.19, $\mathrm{Re}_{U_{\mathrm{jet}}} = 191$ **case and (b)** St = 0.063, $\mathrm{Re}_{U_{\mathrm{jet}}} = 574$ **case.**

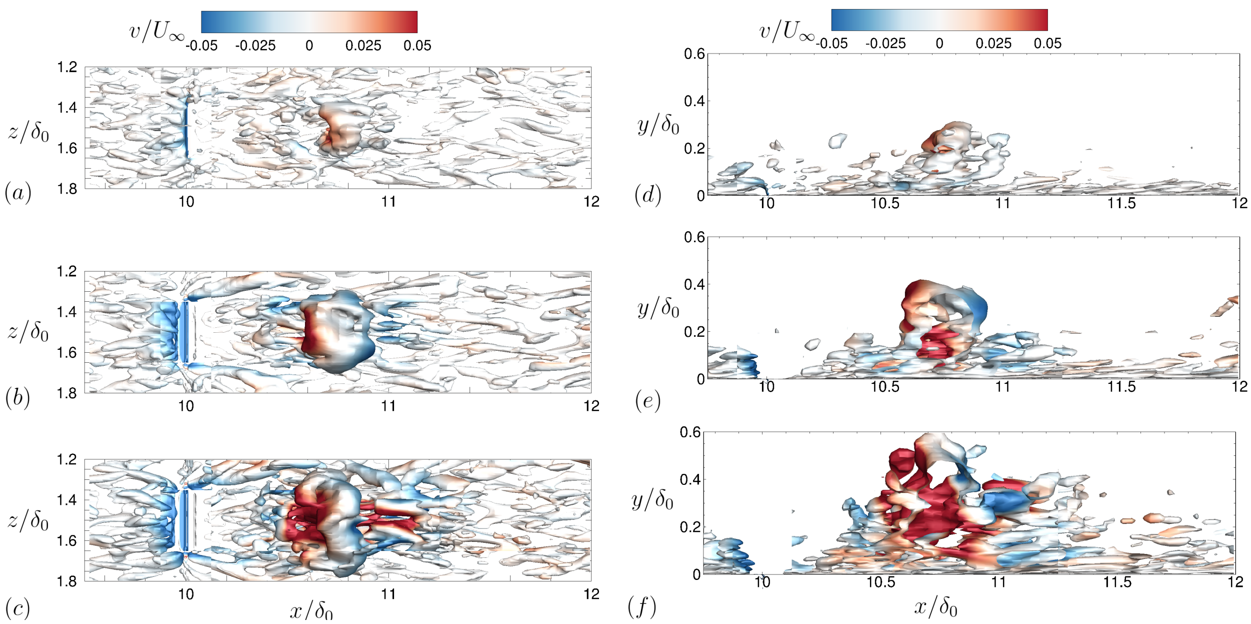

Fig. 7 Top view (a–c) and side view (d–f) of the phase-averaged $Q = 0.01$ **isocontour at** $\phi = 324°$ **for the** $\mathrm{St}_\infty = 0.01$ **case with (a, d)** $r = 0.3$**, (b, e)** $r = 0.6$**, (c, f)** $r = 0.9$**.**

turbulent jets, according to Chen et al. [22], as discussed in the previous subsection. Figs. 7–9 show both a top view and a side view of the 0.01 isocontour of the phase-averaged Q at $\phi = 324°$ (which is near the end of the suction cycle) for all of the cases listed above. The contours are coloured according to the wall-normal velocity to show the regions where fluid is pulled up (red) and down (blue) by the vorticity (i.e. the sense of rotation for the vortex). Due to the limited number of cycles that are practical to average over for the simulations, there is additional unsteady vorticity from the turbulent boundary layer (and jet) that remains.

At $\mathrm{St}_\infty = 0.01$, the main vortical structure that propagates downstream is an isolated horseshoe-like structure which appears like a vortex ring open at the end closest to the wall, as can be seen in Fig. 7a,d. This vortex loop is mainly vertical with a slight tilt downstream. The impact of increasing r seems to be an increase in the penetration height of

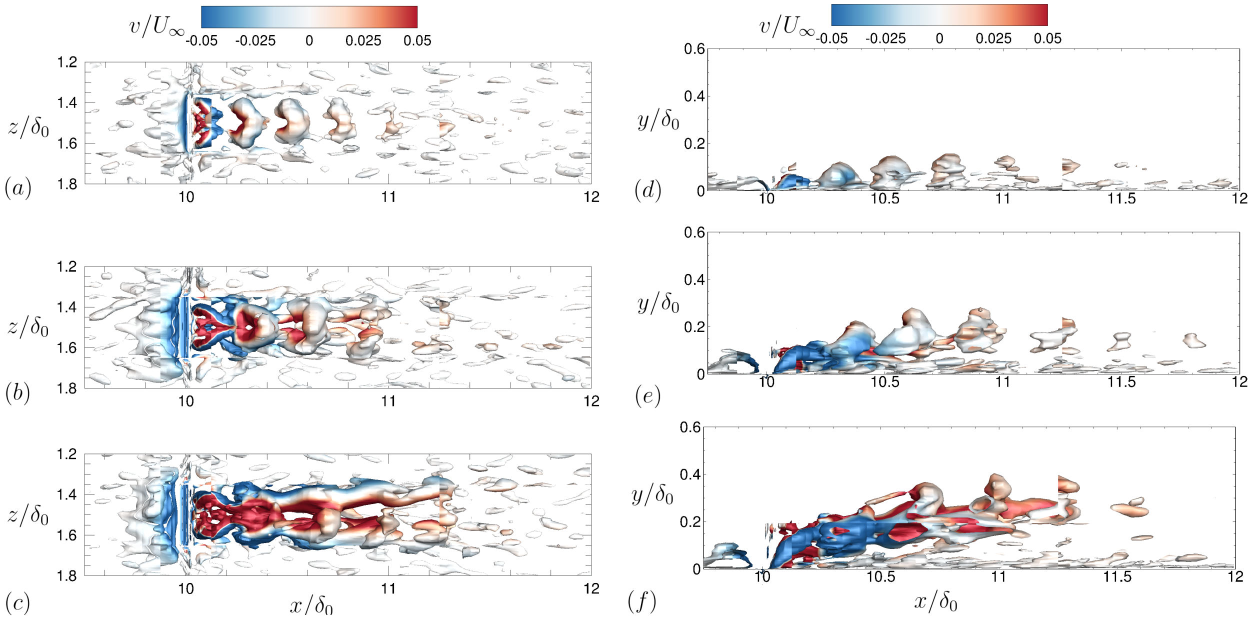

Fig. 8 Top view (a–c) and side view (d–f) of the phase-averaged $Q = 0.01$ isocontour at $\phi = 324°$ for the $\mathrm{St}_\infty = 0.05$ **case with (a, d)** $r = 0.3$**, (b, e)** $r = 0.6$**, (c, f)** $r = 0.9$**.**

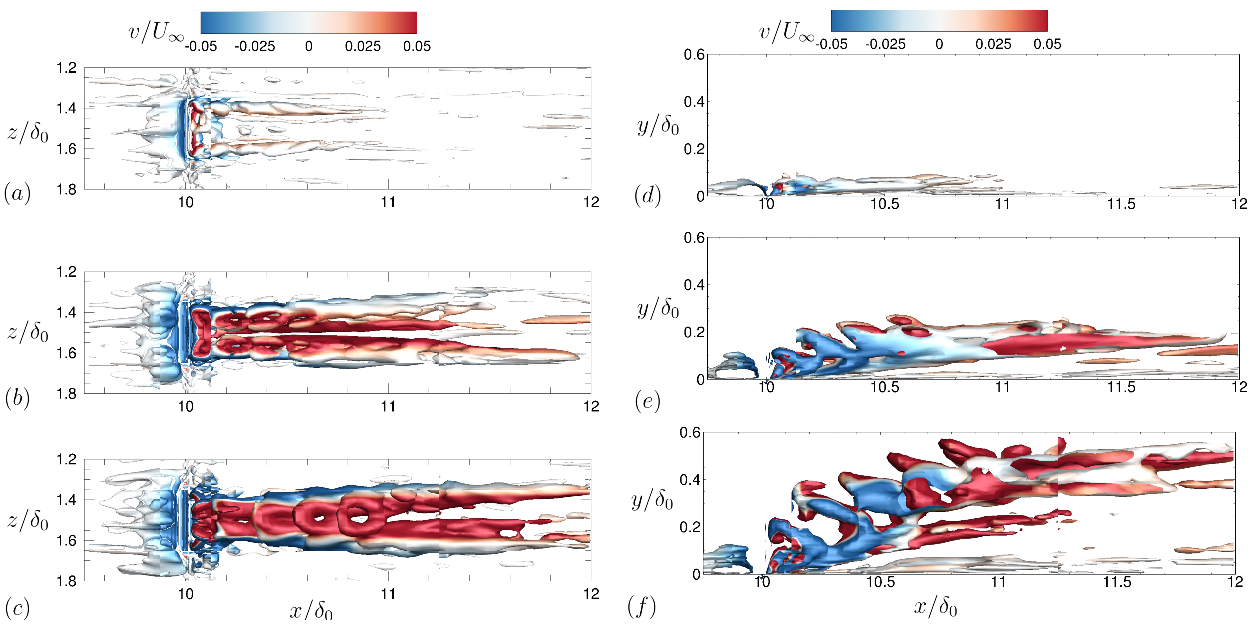

Fig. 9 Top view (a–c) and side view (d–f) of the phase-averaged $Q = 0.01$ isocontour at $\phi = 324°$ for the $\mathrm{St}_\infty = 0.1$ **case with (a, d)** $r = 0.3$**, (b, e)** $r = 0.6$**, (c, f)** $r = 0.9$**.**

this structure along with stronger induced flow. There are also additional streamwise-aligned structures that exist as r is increased which can be seen in Fig 7c,f, in particular. These are either induced by the vortex loop, or are part of the vortex loop that has been stretched due to the interaction of the loop with the crossflow. It is very difficult to pick out the primary vortical structure for this case. This is because, for this particular case, the jet is highly turbulent and so there are a lot of smaller-scale periodic vortical structures associated with the jet.

Increasing to $\mathrm{St}_\infty = 0.05$, at $r = 0.3$, as in Fig. 8a,d, results in a closer spacing of these horseshoe-shaped structures. This train of horseshoe-shaped structures breaks down relatively quickly; after propagating about $1\delta_0$ downstream

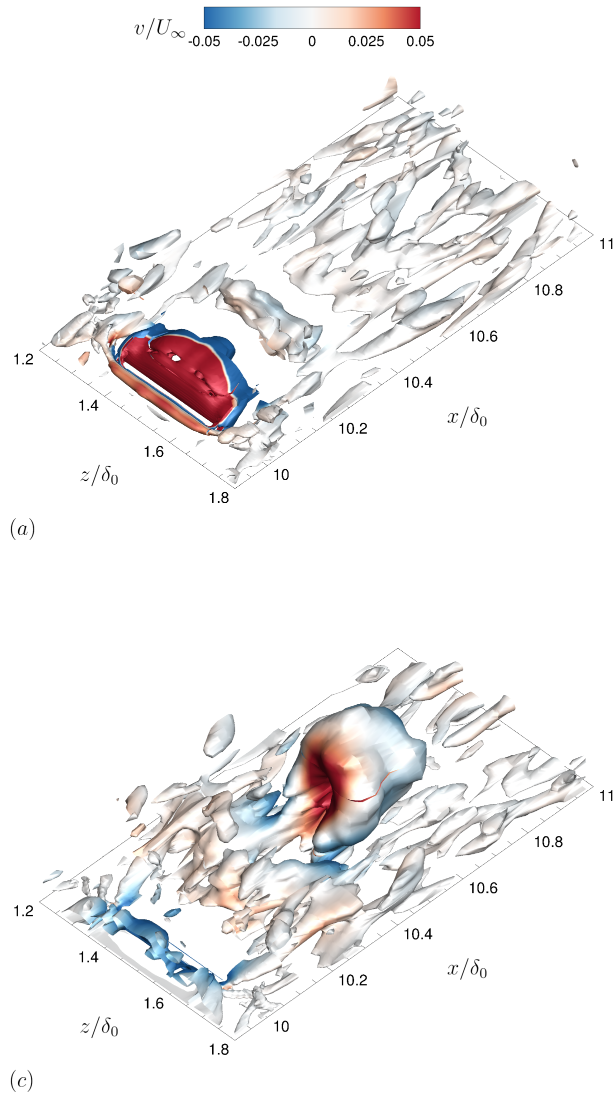

Fig. 10 Phase-averaged $Q = 0.01$ isocontour for the $\mathrm{St}_\infty = 0.01$, $r = 0.3$ case at: (a) $\phi = 104°$, (b) $\phi = 180°$, (c) $\phi = 288°$, and (d) $\phi = 360°$.

of the orifice there is no longer a coherent structure. Aside from an increase in the strength of the induced flow and the penetration height, increasing r at this value of St_∞ causes more modification to the structures than was seen for $\mathrm{St}_\infty = 0.01$. In particular, at $r = 0.9$ (Fig. 8e,f), there is the presence of corrugated quasi-streamwise-aligned structures that persist about $1.5\delta_0$ before breaking apart. This structure appears to be the result of periodic structures merging together.

At $\mathrm{St}_\infty = 0.1$ and $r = 0.3$ (Fig. 9a,d), the dominant downstream vortical structure is a pair of quasi-steady streamwise vortices. This quasi-steady vortex pair agrees with the PIV results of Van Buren et al. [8], which are for a rectangular orifice at a similar St_∞, but larger r. Our results start to differ from those of Van Buren et al. when we increase r. Van Buren et al. saw essentially the same set of quasi-steady streamwise vortices irrespective of r. Meanwhile, we see that as we increase r there is a markedly different structure that results. At $r = 0.6$ (Fig. 9b,e) the initial vortex ring deforms, as was seen for the jet issuing into quiescent flow, and splits into a pair of vortex rings, one at each edge of the orifice, as it propagates downstream. These vortex rings are tilted downstream and eventually merge together at a distance about $1\delta_0$ downstream of the orifice, forming several streamwise-aligned vortices. Similarly, at $r = 0.9$ (Fig. 9c,f), vortex rings also exist as the dominant structures close to the orifice. However, instead of a pair of vortex rings at the edges there is only one vortex ring centered at the centerline of the orifice. With a stronger jet velocity relative to the crossflow,

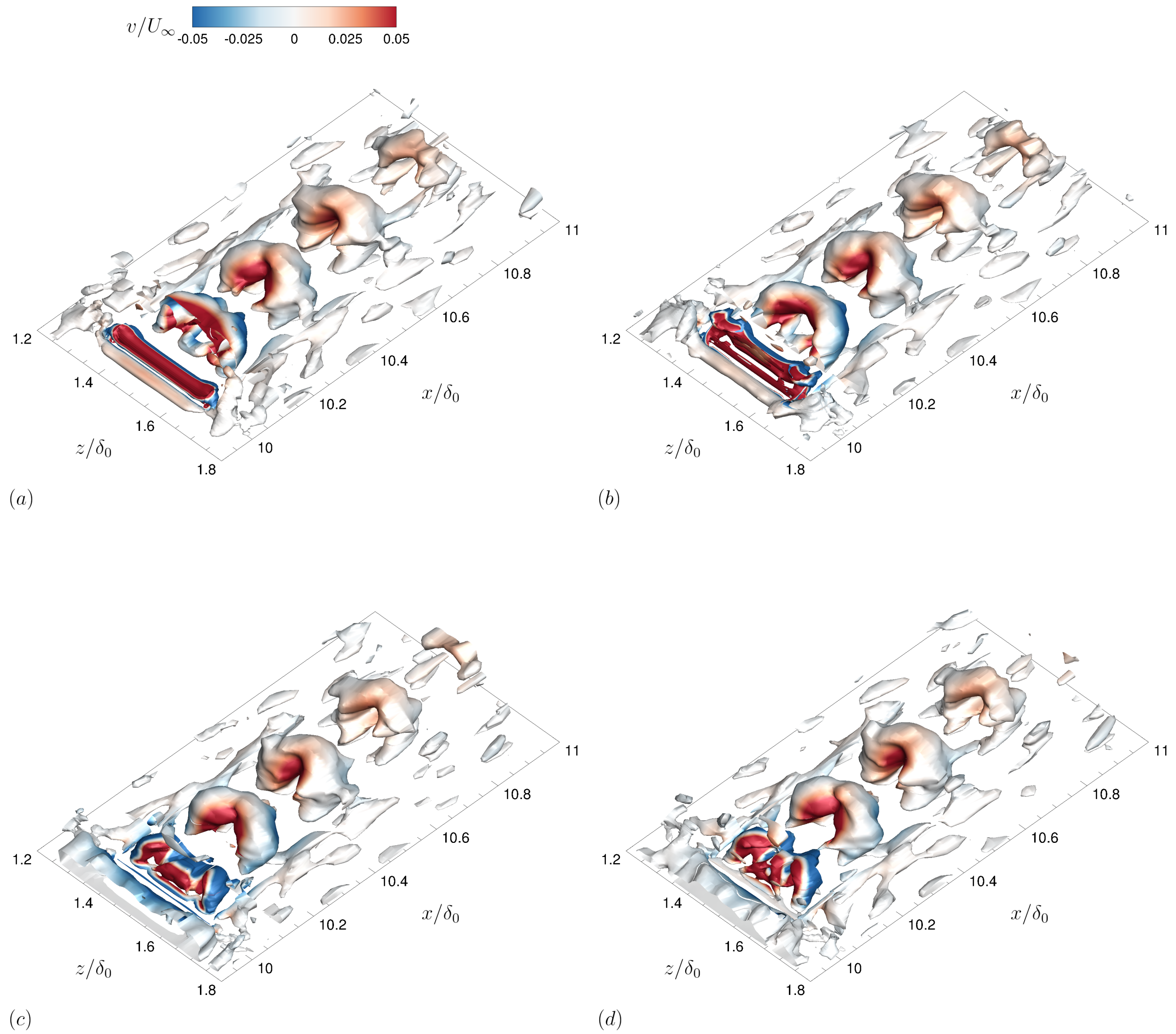

Fig. 11 Phase-averaged $Q = 0.01$ isocontour for the $\mathrm{St}_\infty = 0.05$, $r = 0.3$ case at: (a) $\phi = 104°$, (b) $\phi = 180°$, (c) $\phi = 288°$, and (d) $\phi = 360°$.

the initial vortex ring is able to perform more of its axis switching before being stretched downstream by the crossflow, and as a result the first large vortex ring that is formed is narrower than at $r = 0.6$. Again, the vortex rings merge as they propagate downstream and form a series of quasi-steady streamwise-aligned vortices which persist much further downstream. The presumed reason for the difference between the present study and that of Van Buren et al. is that the isocontours that Van Buren et al. present are for an aspect ratio of 18. A larger aspect ratio means that the vortices at the spanwise edges are further apart and are less able to interact with each other. Furthermore, axis switching has been shown to be much slower with larger aspect ratio orifices [11].

For all of the cases, both the size and penetration of the vortical structures grows as r is increased, and when St_∞ is decreased. An increase in r and a decrease in St_∞ are both consistent with an increase in stroke length L/h. This makes sense to a degree, since the stroke length is a measure of the length of the column of fluid that is expelled during the expulsion stroke. With a larger amount of fluid expelled during the expulsion, there is an increased likelihood that larger vortical structures will be formed, which will penetrate further into the boundary layer.

To elucidate the formation of the various types of dominant vortex structures, Figs. 10 – 12 show the phase evolution for the three cases with $r = 0.3$. The four phases are: $\phi = 104°$ (near peak expulsion), $\phi = 180°$ (between blowing and suction), $\phi = 288°$ (near peak suction), and $\phi = 360°$ (between suction and blowing). Near the orifice, the downstream

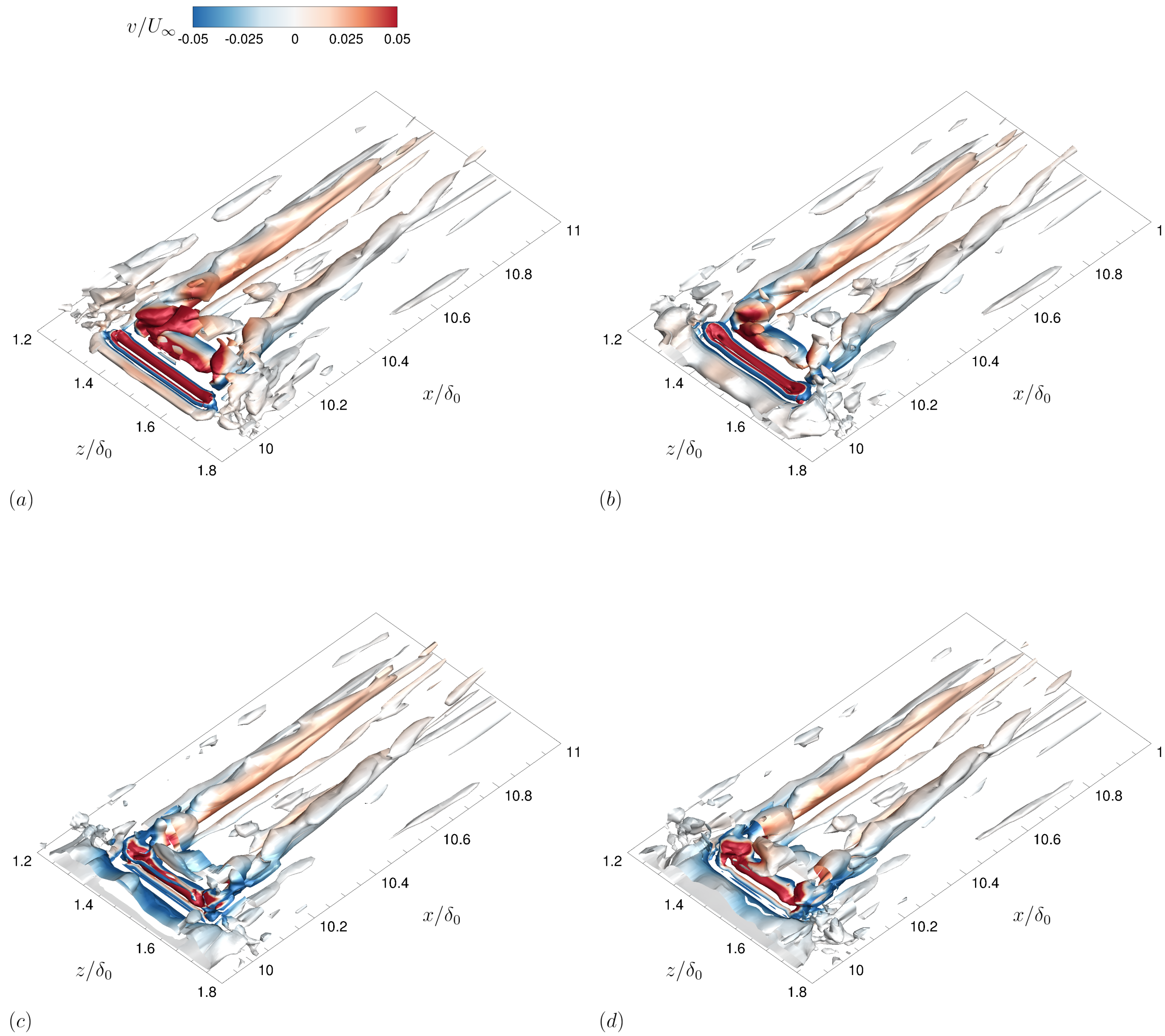

Fig. 12 Phase-averaged $Q = 0.01$ isocontour for the $\mathrm{St}_\infty = 0.1$, $r = 0.3$ case at: (a) $\phi = 104°$, (b) $\phi = 180°$, (c) $\phi = 288°$, and (d) $\phi = 360°$.

spanwise vortex and the two streamwise vortices on either side of the orifice are connected. This is evidenced in the isocontours of Q near the orifice in Fig. 10–12a. For the $\mathrm{St}_\infty = 0.01$ case in Fig. 10, the expulsion stroke is very long. The upstream portion of the vortex ring gets destroyed, while the downstream portion is stretched by the crossflow (Fig. 10a). As this continues to interact with the crossflow, the downstream spanwise vortex is pulled up in the center to form a horsehoe-shaped structure (Fig. 10b), which nearly completes a full vortex ring inclined in the streamwise direction (Fig. 10c,d) as it propagates downstream.

For the $\mathrm{St}_\infty = 0.05$, $r = 0.3$ case in Fig. 11 the end result downstream is horseshoe-shaped vortices similar to the $\mathrm{St}_\infty = 0.01$, $r = 0.3$ case, but the formation mechanism is not the same. For this case, and for the $\mathrm{St}_\infty = 0.1$, $r = 0.3$ case in Fig. 12, a vortex ring is initially formed around the orifice, but the upstream spanwise portion of the ring is killed by the boundary-layer vorticity, such that only the downstream spanwise vortex and the streamwise vortices at the edges survive. As this vortex moves downstream, the intersections of the spanwise and streamwise vortices are pulled up and form horseshoe-shaped vortices on either side of the orifice (Fig. 10b and Fig.11b). These horsehoe-shaped edge vortices could explain the extra streamwise vorticity that appears near the orifice in the experiments and simulations of Sahni et al. [9], which they conjectured to be due to secondary structures. They used a larger aspect ratio ($AR = 21.33$), so there is the possibility of more waviness along the span which could result in additional streamwise vorticity. These edge vortices are also seen when the jet is ejected into quiescent flow, as in Fig. 5, but here the crossflow stretches the vortices in the streamwise direction. For the $St_\infty = 0.05$ case, these two edge vortices merge to form a much larger horseshoe-shaped structure which extends across the span of the jet slot (Fig. 11c) and grows as it convects downstream (Fig. 11d). This is much wider and has shorter legs than for $St_\infty = 0.01$. For $St_\infty = 0.1$, the two edge vortices start to merge (see the second vortex downstream of the slot in Fig. 12d), but then the interior legs dissipate while the outer legs remain intact further downstream (seen as one looks downstream at successive cycles in each of Fig. 12a-d). The outer legs of these structures merge together over successive cycles and form the quasi-steady streamwise vortex pair that is prevalent far downstream of the orifice. There also appear to be steady streamwise vortices closer to the centerline of the orifice induced by the main steady streamwise vortices.

Comparing the three sets of structures in Figs. 10 – 12, it is also clear that the strength of the induced vertical flow increases with reduced St_∞. Thus, one would expect that the impact of the vortical structure on the boundary layer is strongest for $St_\infty = 0.01$ and weakest for $St_\infty = 0.1$. However, due to the quasi-steady structure for $St_\infty = 0.1$, it is affecting the boundary layer at all phases in the jet cycle, while for $St_\infty = 0.1$, with its isolated structure, the impact is larger, but only for a small portion of the cycle when the structure passes a particular streamwise location in the boundary layer.

V. Conclusions

The downstream development of the vortices emitted through the rectangular orifice of a synthetic jet actuator into a turbulent boundary layer depends on both the Strouhal number, or frequency, and blowing ratio, or amplitude, of the actuation. At high St_∞ and $r = 0.3$, we have shown that the dominant structure downstream of the orifice is a pair of quasi-steady streamwise vortices. As St_∞ is decreased, this eventually transitions to a regime where horseshoe-shaped vortical structures are the dominant feature. These can be formed in two ways: either edge vortices pull up into horseshoe-shaped structures that merge to form a larger horseshoe, or vorticity from a long expulsion stroke is directly pulled into a horseshoe-shaped vortical structure. A large variety of structures is also possible as r is increased due to the increased penetration and jet velocity relative to the local flow. With a stronger jet flow relative to the local flow the jet approaches quiescent conditions. It starts to switch axes, to varying degrees based on r, before being stretched downstream by the boundary layer flow. This fundamental knowledge of the vortex structure will be useful when designing and interpreting the results of future flow control studies, such as separation control and skin-friction drag reduction in a turbulent boundary layer involving synthetic jets emanating from spanwise-oriented orifices.

Acknowledgements

The authors would like to acknowledge the financial support of the Natural Sciences and Engineering Research Council of Canada.

References

[1] Fric, T. F., and Roshko, A., "Vortical structure in the wake of a transverse jet," *Journal of Fluid Mechanics*, Vol. 279, 1994, pp. 1–47.

[2] Sau, R., and Mahesh, K., "Dynamics and mixing of vortex rings in crossflow," *Journal of Fluid Mechanics*, Vol. 604, 2008, pp. 389–409.

[3] Cater, J. E., and Soria, J., "The evolution of round zero-net-mass-flux jets," *Journal of Fluid Mechanics*, Vol. 472, 2002, pp. 167–200.

[4] Gharib, M., Rambod, E., and Shariff, K., "A universal time scale for vortex ring formation," *Journal of Fluid Mechanics*, Vol. 360, 1998, pp. 121–140.

[5] Jabbal, M., Wu, J., and Zhong, S., "The performance of round synthetic jets in quiescent flow," *The Aeronautical Journal*, 2006, pp. 385–393.

[6] Holman, R., Utturkar, Y., Mittal, R., Smith, B. L., and Cattafesta, L., "Formation criterion for synthetic jets," *AIAA Journal*, Vol. 43, 2005, pp. 2110–2116.

[7] Jabbal, M., and Zhong, S., "The near wall effect of synthetic jets in a boundary layer," *International Journal of Heat and Fluid Flow*, Vol. 29, 2008, pp. 119–130.

[8] Van Buren, T., Beyar, M., Leong, C. M., , and Amitay, M., “Three-dimensional interaction of a finite-span synthetic jet in a crossflow,” *Physics of Fluids*, Vol. 28, 2016, p. 037106.

[9] Sahni, O., Wood, J., Jansen, K. E., and Amitay, M., “Three-dimensional interactions between a finite-span synthetic jet and a crossflow,” *Journal of Fluid Mechanics*, Vol. 671, 2011, pp. 254–287.

[10] Amitay, M., and Cannelle, F., “Evolution of finite span synthetic jets,” *Physics of Fluids*, Vol. 18, 2006, p. 054101.

[11] Van Buren, T., Whalen, E., and Amitay, M., “Vortex formation of a finite-span synthetic jet: effect of rectangular orifice geometry,” *Journal of Fluid Mechanics*, Vol. 745, 2014, pp. 180–207.

[12] Smith, B. L., and Glezer, A., “The formation and evolution of synthetic jets,” *Physics of Fluids*, Vol. 10, 1998, pp. 2281–2297.

[13] Hicken, J. E., and Zingg, D. W., “Parallel Newton-Krylov solver for the Euler equations discretized using simultaneous approximation terms,” *AIAA Journal*, Vol. 46, No. 11, 2008, pp. 2773–2786.

[14] Osusky, M., and Zingg, D. W., “Parallel Newton-Krylov-Schur flow solver for the Navier-Stokes equations,” *AIAA Journal*, Vol. 51, No. 12, 2013, pp. 2833–2851.

[15] Boom, P. D., Rolston, S., and Zingg, D. W., “Large-eddy simulation of controlled and uncontrolled turbulent boundary layers,” *Tenth International Conference on Computational Fluid Dynamics*, Barcelona, Spain, 2018. ICCFD Paper 10-2018-156.

[16] Lund, T. S., Wu, X., and Squires, K. D., “Generation of turbulent inflow data for spatially-developing boundary layer simulations,” *Journal of Computational Physics*, Vol. 140, 1998, pp. 223–258.

[17] Raju, R., Aram, E., Mittal, R., and Cattafesta, L., “Simple models of zero-net mass-flux jets for flow control simulations,” *International Journal of Flow Control*, Vol. 1, 2009, pp. 179–197.

[18] Schlatter, P., and Örlu, R., “Assessment of direct numerical simulation data of turbulent boundary layers,” *Journal of Fluid Mechanics*, Vol. 375, 2010, pp. 116–126.

[19] Berk, T., Hutchins, N., Marusic, I., and Ganapathisubramani, B., “Trajectory of a synthetic jet issuing into high-Reynolds-number turbulent boundary layers,” *Journal of Fluid Mechanics*, Vol. 856, 2018, pp. 531–551.

[20] Smith, D. R., “Interaction of a synthetic jet with a crossflow boundary layer,” *AIAA Journal*, Vol. 40, No. 11, 2002, pp. 2277–2288.

[21] Ravi, B. R., Mittal, R., and Najjar, F. M., “Study of three-dimensional synthetic jet flowfields using direct numerical simulation,” *42nd AIAA Aerospace Sciences Meeting and Exhibit*, Reno, N.V., 2004. AIAA Paper 2004-0091.

[22] Chen, F.-J., Yao, C., Beeler, G., Bryant, R., and Fox, R., “Development of synthetic jet actuators for active flow control at NASA Langley,” *Fluids 2000 Conference and Exhibit*, 2000. AIAA Paper 2000-2405.